Journal of Applied Physics ARTICLE pubs.aip.org/aip/jap

Mode-resolved phonon transmittance using lattice dynamics: Robust algorithm and statistical characteristics

Cite as: J. Appl. Phys. 134, 155302 (2023); doi: 10.1063/5.0171201
Submitted: 7 August 2023 · Accepted: 27 September 2023 ·
Published Online: 17 October 2023

Hong-Ao Yang and Bing-Yang Cao[a)]

AFFILIATIONS

Key Laboratory for Thermal Science and Power Engineering of Ministry of Education, Department of Engineering Mechanics, Tsinghua University, Beijing 100084, China

[a)]Author to whom correspondence should be addressed: caoby@tsinghua.edu.cn. Tel/Fax: +86-10-6279-4531.

ABSTRACT

Lattice dynamics (LD) enables the calculation of mode-resolved transmittance of phonons passing through an interface, which is essential for understanding and controlling the thermal boundary conductance (TBC). However, the original LD method may yield unphysical transmittance over 100% due to the absence of the constraint of energy conservation. Here, we present a robust LD algorithm that utilizes linear algebra transformations and projection gradient descent iterations to ensure energy conservation. Our approach demonstrates consistency with the original LD method on the atomically smooth Si/Ge interface and exhibits robustness on rough Si/Ge interfaces. The evanescent modes and localized effects at the interface are revealed. In addition, bottom-up analysis of the phonon transmittance shows that the anisotropy in the azimuth angle can be ignored, while the dependency on the frequency and polar angle can be decoupled. The decoupled expression reproduces the TBC precisely. This work provides comprehensive insights into the mode-resolved phonon transmittance across interfaces and paves the way for further research into the mechanism of TBC and its relation to atomic structures.

I. INTRODUCTION

Thermal boundary conductance (TBC) is crucial for the thermal management of microelectronics,[1,2] nanocomposites,[3] thermal electronics,[4] and optoelectronics.[5] As manufacturing processes continue to evolve toward miniaturization, the density of interfaces within devices is experiencing a rapid surge. The TBC has become dominant in total thermal resistance. The TBC at solid interfaces, which is affected by many factors, such as roughness,[6–8] bonding strength,[9] and defects,[10] has attracted immense interest. Phonons govern the TBC in semiconductors since they are the primary heat carriers. A comprehensive description of the behavior of phonons at interfaces has long been a common pursuit.

The Landauer formula offers an intuitive explanation of the TBC by summing over the contribution from each phonon mode,[11]

$$G = \frac{1}{V}\sum_{q,\nu} \hbar\omega_{q\nu} v_{q\nu,z} T_{q\nu} \frac{\partial f}{\partial T}, \quad (1)$$

in which V is the volume of the primitive cell, q is the phonon wave vector, ν is the phonon band index, $\omega_{q\nu}$ is the angular frequency of phonon qν, $v_{q\nu,z}$ is the z component of the group velocity of phonon qν, $T_{q\nu}$ is the transmittance of phonon qν, f is the Bose–Einstein distribution function, and T is the temperature. Among them, other quantities are easily obtainable, while the mode-resolved transmittance is challenging to determine. An easier but less accurate method is to approximate T as a function of ω, i.e., $T \approx T(\omega)$, known as the spectral transmittance. In the last century, two continuum models were developed to determine the spectral transmittance. One is the acoustic mismatch model (AMM), assuming specular reflection and transmission.[12] The other is the diffuse mismatch model (DMM), assuming the opposite extreme, where all phonons experience diffusive scattering.[13] Subsequently, several modifications were made to the DMM. The exact phonon dispersion was adopted to replace the Debye model.[14,15] The effects of disorder were included by introducing a virtual crystal of finite thickness at the interface.[16] The inelastic scattering was also incorporated into the DMM.[17] The frequency-resolved phonon transmittance has been verified by experiments.[18,19] However, the convention of the spectral transmittance remains unchanged.

Several numerical approaches have been developed to compute the spectral transmittance. The atomistic Green's function (AGF) method uses the second-order force constants at the interface as input and computes the TBC in the reciprocal space and frequency domain.[20,21] The traditional AGF was formulated in the harmonic regime, while anharmonic terms were incorporated recently.[22,23] On the other hand, molecular dynamics (MD) inherently involves full-order anharmonic terms. Spectral TBC can be extracted from the Fourier transform of atomistic heat flux across the interface in non-equilibrium molecular dynamics (NEMD).[24–27]. Based on the fluctuation-dissipation theory, spectral TBC can be computed in equilibrium molecular dynamics (EMD) using the Green–Kubo formula.[28,29] The main disadvantage of MD simulation is that it cannot account for quantum effects, thus being inaccurate at low temperatures and low phonon occupancy. In addition, MD is constrained by size effects.[30] Both AGF and MD are limited to calculating frequency-dependent TBC. Recently, AGF was extended to compute the transmittance of a single phonon mode by solving the eigensystem of the interfacial Hamiltonian matrix.[31–35] This method first constructs the Bloch matrix and then obtains discrete wave vectors by diagonalizing the matrix and calculating the phase of the eigenvalues with unit norms. The phonons cannot be sampled uniformly since the wave vectors are determined post hoc. Therefore, the single-mode AGF is not conducive to practical applications. The investigation of mode-resolved phonon transmittance remains insufficient in the current state of research.

The lattice dynamics (LD) is a useful approach for calculating mode-resolved phonon transmittance, also known as the scattering boundary method (SBM).[11] While not a recent development, it has yet to reach its full potential. LD is considered a mathematical equivalent to AGF[33] since it uses the same input as the AGF method. However, LD shows superiority in single-mode calculations by incorporating phase information on the boundaries, whereas AGF only utilizes density information. The prototype of LD was proposed in 1978 when Lumpkin et al. computed the TBC of a one-dimensional atomic chain analytically.[36] Later, this method was implemented on a 3D face-centered cubic lattice[37] and a Si/Ge interface with a diamond structure.[38] Soon after, the solution transitioned from analytical to numerical. Wang et al. computed the phonon transmittance of acoustic branches in a nanotube junction,[39] in which the equations of motion were assembled into an overdetermined linear system of equations. The linear system was approximately solved using the singular value decomposition (SVD) method. Subsequently, the LD method was applied to atomic junctions[40] and superlattice junctions,[41] while the algorithm itself has not advanced further. However, the current LD method lacks the constraint of energy conservation, thus producing non-physical results. As can be seen in the literature, the transmittance and reflectance do not sum up to unity.[42] Although other studies did not mention reflectance explicitly,[39,41] the energy conservation issue still lurks in the background. This issue arises from the numerical error when solving the overdetermined equations approximately.[43] The problem becomes even more pronounced when dealing with non-atomically smooth interfaces as additional interfacial atoms and phonon modes need to be taken into consideration. Hence, there is currently no research applying LD methods to rough interfaces. The absence of the constraint on energy conservation becomes a major obstacle in applying the LD approach to realistic interfaces.

In this work, we address the issue of constraint missing in the original LD method. We begin by using linear algebra transformations to reduce the number of variables and then apply energy conservation constraints, utilizing the projection gradient descent method for iterative solutions. The modified method is tested on an atomically smooth interface and two types of rough interfaces taking into account the contributions of diffusive scattering modes and demonstrates excellent robustness. Furthermore, the localized effects induced by the interface are accurately captured. The existence of evanescent modes is revealed. Finally, the statistical characteristics of transmittance are analyzed using a bottom-up approach. It is found that the anisotropy in the azimuth angle can be ignored, while the dependency on the frequency and polar angle can be decoupled. The decoupled expression reproduces the TBC precisely.

II. METHODOLOGY

A. Robust lattice dynamics approach

We begin by providing a clear definition of the system under investigation. The system we discuss involves two periodic crystals in contact at an interface. On either side of the interface, the crystal exhibits periodicity that extends infinitely. In the vicinity of the interface, the arrangement of atoms is arbitrary, allowing for various types of rough interfaces. The entire system is divided into three sections: the left lead (L), the device (D), and the right lead (R). The left and right leads are half-infinite. The thickness of the device should be sufficiently large to cover all the localized effects. Specific requirements regarding the thickness of the device will be addressed in a subsequent discussion. We assume the harmonic interatomic interaction so that only harmonic phonon scattering is allowed, i.e., the scattered phonons have the same frequency as the incident phonon.

The system is governed by Newton's equations of motion. Under the assumption of harmonic interatomic interaction, Newton's equation of motion of atom i is written as

$$\sum_j \Phi_{ij} u_j = m_i \frac{d^2 u_i}{dt^2}, \tag{2}$$

where Φ_{ij} is the second-order force constant between atom i and j, u_i is the displacement of atom i, and m_i is the mass of atom i. In bulk crystals, the harmonic approximation directly leads to the eigensystem of phonons,

$$H_q s_{q\nu} = \omega_{q\nu}^2 s_{q\nu}, \tag{3}$$

where q is the phonon wave vector, ν is the phonon band index, H_q is the Hamiltonian at q, $s_{q\nu}$ is the phonon eigenvector, and $\omega_{q\nu}$ is the phonon frequency. The left lead and the right lead can be treated as ideal crystals in regions far away from the interface. Consequently, the motion of the atoms in both leads can be described by phonons in bulk crystals.

The next step is to determine the transmittance of a particular phonon mode, denoted as I. We assume that the incident phonon

originates from the left lead, and the derivation applies in the opposite direction. A portion of the energy carried by the incident phonon is reflected back to the left lead, while the remaining energy is transmitted to the right lead. Phonon modes involved in reflection and transmission dissipate into bulk phonon modes on both sides, as only these modes are allowed in the crystals. Any atomic vibration can be decomposed into a combination of multiple bulk phonon modes. We denote reflection modes as R_j and transmission modes as T_k. Due to the harmonic interatomic interaction, R_j and T_k have the same frequency as the incident mode. Due to the translational symmetry in the parallel interface direction, R_j and T_k have the same horizontal component of crystal momentum as the incident phonon mode. The identification of these allowed modes will be detailed in Sec. II B. Based on the aforementioned discussion, the atomic motion on the left lead can be represented as the superposition of I and R_j, while the atomic motion on the right side can be represented as the superposition of T_k. No assumptions are made about the atomic motion in the device. They are variables to be determined. In such a scenario, the displacements of atoms are

$$\begin{aligned} u_i &= s_I e^{iq_I \cdot r_i} + \sum_{R_j} A_{R_j} s_{R_j} e^{iq_{R_j} \cdot r_i}, && i \in L, \\ u_i &\text{ is to be solved}, && i \in D, \\ u_i &= \sum_{T_k} A_{T_k} s_{T_k} e^{iq_{T_k} \cdot r_i}, && i \in R, \end{aligned} \tag{4}$$

in which A_{R_j} is the amplitude of the reflection mode R_j and A_{T_k} is the amplitude of the transmission mode T_k. We assume the amplitude of the incident mode is 1 for simplicity. The phase factor $e^{i\omega t}$ in Eq. (4) is omitted since I, R_j, and T_k have the same frequency. The transmittance T is defined as the energy flux density ratio between the transmission modes and the incident mode. The reflectance R is defined similarly. That is,

$$\begin{aligned} T &= \sum_{T_k} \frac{v_{T_k,z}}{v_{I,z}} |A_{T_k}|^2, \\ R &= \sum_{R_j} \frac{-v_{R_j,z}}{v_{I,z}} |A_{R_j}|^2, \end{aligned} \tag{5}$$

where v is the group velocity. The law of conservation of energy requires that

$$T + R = 1. \tag{6}$$

Although the constraint of energy conservation is not explicitly stated in Eq. (4), it is an inherent requirement in the physical context.

Thus far, we have elucidated the physical characteristics of the system. Now, let us distill the mathematical equations governing the system. Note that any linear combination of phonon eigenvectors in the bulk satisfies Newton's equation of motion. Hence, the left lead and right lead components in Eq. (4) automatically satisfy Eq. (2). Therefore, there remain the displacements of atoms in the device, the amplitudes of the reflection modes, and the amplitudes of the transmission modes to be solved. They are divided into two categories, defined as

$$\begin{aligned} x_1 &= \{u_i,\ i \in D\}, \\ x_2 &= \{A_{R_1}, \ldots, A_{R_{jmax}}, A_{T_1}, \ldots, A_{T_{kmax}}\}. \end{aligned} \tag{7}$$

By substituting Eq. (4) into Eq. (2), we can obtain a system of linear equations in terms of x_1 and x_2,

$$A_1 x_1 + A_2 x_2 = b, \tag{8}$$

where A_1, A_2, and b are coefficient matrices. The number of equations exceeds the number of variables, making the set of equations overdetermined. This occurs because the evanescent modes are not considered.[43] Nevertheless, assuming all evanescent modes decay to zero within the device, the overdetermined set of equations is still consistent. This kind of problem is known as linear least squares. The solution can be obtained by minimizing the residual,

$$r = |b - A_1 x_1 - A_2 x_2|. \tag{9}$$

Next, we will present the methodology for solving this mathematical equation. The original LD method did not take into account the energy conservation constraint during the solving process, whereas our approach incorporates the energy conservation constraint. In the original LD method, the residual is minimized by finding the linear least square solution of the following equation using the singular value decomposition (SVD) method:

$$\begin{pmatrix} A_1 & 0 \\ 0 & A_2 \end{pmatrix} \begin{pmatrix} x_1 \\ x_2 \end{pmatrix} = b, \tag{10a}$$

$$\begin{pmatrix} A_1 & 0 \\ 0 & A_2 \end{pmatrix} = USV^*, \tag{10b}$$

$$\begin{pmatrix} x_1 \\ x_2 \end{pmatrix} = VS^{-1}U^* b. \tag{10c}$$

It can be seen that x_1 and x_2 are solved simultaneously. The numerical error of x_2 is significantly large for two reasons. First, no constraint of energy conservation is applied to x_2. Second, the dimension of x_1 is three times the number of atoms in the device, which is much larger than x_2. As a result, numerical errors can lead to a large variation in the amplitudes of reflection and transmission modes, further resulting in energy non-conservation and inaccurate calculation of transmittance. The specific consequences arising from errors will be elucidated in Sec. III.

In our robust algorithm, Eq. (9) is minimized with the constraint in Eq. (6). Since the constraint only applies to x_2, we optimize x_1 and x_2 sequentially to minimize r,

$$r_{min} = \min_{x_2} \min_{x_1} |(b - A_2 x_2) - A_1 x_1|. \tag{11}$$

The variable x_1 can be eliminated by the following steps. First, perform a QR decomposition on A_1,

$$A_1 = QR, \tag{12}$$

in which Q is the orthogonal and R is the upper triangular. Then, the optimized x_1 is given by

$$x_1 = R^{-1}Q^*(b - A_2x_2), \tag{13}$$

in which the star sign stands for conjugate transpose. The minimal r is

$$\begin{aligned} r_{min} &= \min_{x_2}\min_{x_1}|(b - A_2x_2) - A_1x_1| \\ &= \min_{x_2}|(b - A_2x_2) - QRR^{-1}Q^*(b - A_2x_2)| \\ &= \min_{x_2}|(I - QQ^*)b - (I - QQ^*)A_2x_2| \\ &= \min_{x_2}|b_{eff} - A_{eff}x_2|, \end{aligned} \tag{14}$$

where $b_{eff} = (I - QQ^*)b$ and $A_{eff} = (I - QQ^*)A_2$. To this point, r_{min} depends only on x_2 and can be considered as another linear least square problem. This least square problem has reduced its dimensionality by several orders of magnitude compared to the previous least squares problem. However, this problem cannot be solved using the SVD or QR method because of the existence of the constraint of energy conservation. Other all-purpose minimization techniques, such as constrained conjugate gradients, also perform poorly due to the large dimension of the problem.

We utilize the projected gradient descent (PGD) for constrained optimization. PGD is the most common and efficient method for iteratively solving constrained linear least squares.[44] Upon revisiting the constraint Eq. (6), we can observe that it is an elliptical equation, which can be transformed into a unit-norm equation (a circle) by linearly scaling the variables. Therefore, we will refer to the constraint as $\|x_2\|_2 = 1$ for simplicity. The PGD algorithm operates as follows:

$$\begin{aligned} x_2^{(k+1)} &= x_2^{(k)} - \eta A_{eff}^T\left(A_{eff}x_2^{(k)} - b_{eff}\right), \\ x_2^{(k+1)} &= x_2^{(k+1)}/\|x_2^{(k+1)}\|_2, \end{aligned} \tag{15}$$

in which η is the step width. To achieve linear convergence,[45] η is chosen as

$$\eta = 1/(\|A_{eff}\|_2\|b_{eff}\|_2): \tag{16}$$

We start the iteration from a random $x_2^{(0)}$ and stop until the difference in residual of adjacent iterations is smaller than 1×10^{-9}. The speed of convergence and the ability to find global minima will be discussed later. Once the convergence is achieved, the transmittance can be obtained from Eq. (5). Subsequently, the TBC can be calculated using the Landauer formula Eq. (1). A uniform sampling of phonon wave vectors in the first Brillouin zone on a $20 \times 20 \times 20$ mesh grid is employed, which is sufficient for the system under investigation.

It is worth noting that the size effect in the LD method is entirely different from that in the NEMD method. In NEMD, the size effect arises from boundary scattering caused by the simulation box,[46] which is inevitable in molecular dynamics simulations. Consequently, the characteristic length of the simulation box must exceed the phonon mean free path (MFP). Conversely, the LD method does not involve boundary scattering. Instead, sufficient device thickness is still required to eliminate the exponentially decaying evanescent mode, which is significantly shorter than the phonon MFP. The evanescent mode is an inherent characteristic caused by the presence of interfaces, and it cannot be avoided in any method. A more detailed discussion on evanescent modes will be provided in Sec. III.

B. Determination of diffusive scattering modes

In previous research using the original LD method, it was always assumed that phonons undergo specular scattering. When dealing with atomically smooth interfaces, considering only specular scattering is reasonable. However, in the case of rough interfaces, it becomes necessary to account for diffusive scattering as well. Due to the inherent roughness of realistic interfaces, the original LD method is not applicable in the real world.

Under the assumption of specular scattering, the reflection and transmission phonon modes have the same horizontal component of crystal momentum as the incident phonon mode. If we assume that the interface is situated on the xy plane, the specular scattering hypothesis states that

$$q_{T,xy} = q_{R,xy} = q_{I,xy}: \tag{17}$$

The z component of the phonon wave vector is solved by the elastic scattering assumption,

$$\omega(q_T, \nu_T) = \omega(q_R, \nu_R) = \omega(q_I, \nu_I): \tag{18}$$

To account for the diffusive scattering, we replicate the unit cell horizontally to construct a supercell and then perturb the positions of atoms near the interface to introduce roughness. The system exhibits periodicity in the horizontal direction with respect to the lattice vectors of the supercell. Any horizontal wave vectors that differ by a multiple of the horizontal reciprocal lattice vectors of the supercell are permitted, that is,

$$\begin{aligned} q_{T,xy} &= q_{I,xy} + c_1G_1 + c_2G_2, \\ q_{R,xy} &= q_{I,xy} + c_3G_1 + c_4G_2, \end{aligned} \tag{19}$$

where $c_{1,2,3,4}$ are integers and $G_{1,2}$ are horizontal reciprocal lattice constants of the supercell. Then, the z component of the wave vector is determined according to Eq. (18) while ensuring that the wave vector lies within the first Brillouin zone to avoid duplicate counting. A similar strategy has been adopted in the literature,[33,47] but it has not been implemented in the lattice dynamics.

C. Simulation details

The Si/Ge interface along the [001] interface is chosen for the case study. This particular type of interface has been extensively studied in the literature using the MD,[11,48] AGF,[49] and LD methods.[38] Researchers have also placed particular focus on the diffusive scattering at rough interfaces[33] and the mode-resolved transmission properties at special points on ideal interfaces.[22] However, there are currently no reports on the mode-resolved phonon

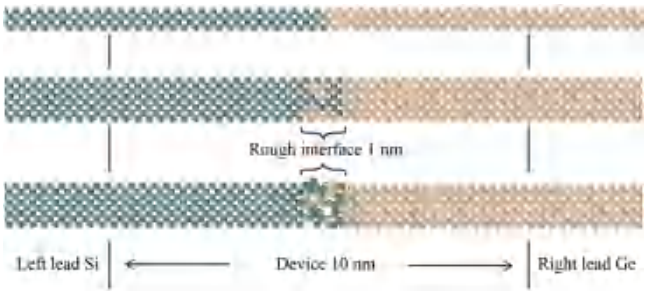

FIG. 1. Schematic diagram of the three interface types. The top panel represents the atomically smooth interface. The middle panel represents the interdiffusion interface. The bottom panel represents the amorphous interface. The latter two interfaces are constructed with a 2×2 supercell and 1 nm roughness. The thickness of the device is set to 10 nm in all three models.

transmittance at the rough Si/Ge interface using the LD method. Our work will serve to contrast and complement existing literature in the field.

We define that the interface normal is along the z direction. The Tersoff potential[50] is adopted for calculating interatomic forces. As Si and Ge have different lattice constants, we posit that Si remains unstressed. Ge maintains the same lattice constant as Si in the xy direction and is extended in the z direction to release the stress in the z direction. The lattice constant of Si is $a = 5{:}432$ Å. The lattice constants of Ge are $a = 5{:}432$ Å and $c = 5{:}815$ Å. The phonon dispersion of bulk Si and strained bulk Ge are computed using the Phonopy package.[51]

Three types of interfaces are constructed, as shown in Fig. 1. The first is an atomically smooth interface, in which the Si lead and the Ge lead are directly contacted. The second type is interdiffusion interfaces, obtained by first repeating the system by 2×2 in the xy direction and randomly swapping 50% of the atoms within 1 nm near the interface. The third type is amorphous interfaces, achieved by initially repeating the system by 2×2 in the xy direction and then using molecular dynamics to displace the atoms within 1 nm near the interface while keeping the rest of the atoms fixed. A Langevin thermostat at 3000 K, 1 fs time step, and 1×10^6 total steps are employed in the molecular dynamics. Subsequently, the structure is quenched to the ground state. It should be noted that in all three types, the final structure is optimized to ensure that all atoms are at their equilibrium positions. Finally, the second-order force constants are computed using a central difference method. Once the interface structures have been constructed, the system is partitioned into three regions along the z direction: the left lead, the device, and the right lead. To ensure that any localized effects resulting from the interface are adequately captured, the device must be sufficiently thick. In our calculations, we set the length of the device to 10 nm if no other value is specified. This value is sufficient for all localized effects, which will be discussed in Sec. III.

III. RESULTS AND DISCUSSION

We first present the calculation results of TBC. Table I summarizes the TBC of three types of Si/Ge interfaces at 300 K, as well as the TBC of the atomically smooth interface calculated using the original LD method and from the literature. The TBC of an atomically smooth Si/Ge interface is 324 $MW/m^2 K$, which is in good agreement with the results of the original LD method,[38] the AGF method,[49] and the NEMD simulation.[11] Both interdiffusion interfaces and amorphous interfaces can cause a decrease in TBC, with amorphous interfaces leading to a greater decrease. The original LD failed to compute the TBC of rough interfaces, manifested as yielding TBCs several orders of magnitude greater than expected. Without the constraint of energy conservation, the sum of transmittance and reflectance was not limited to 1. Figure 2 displays the histogram of the sum of transmittance and reflectance for each phonon mode on the sampling mesh. It can be observed that the energy non-conservation issue is more pronounced in rough interfaces. Although most phonon modes roughly obey the rule of energy conservation, numerous exceptions exist. In rough interfaces, some phonon modes exhibit transmittance several orders of magnitude higher than 1, leading to the failure of TBC calculations. This failure emphasizes the need for the constraint of energy conservation, which is fulfilled in our method.

The constraint of energy conservation is achieved by constrained PGD iteration in our method. The convergence of PGD iteration and the ability to find the global minimum is evaluated by examining the iteration process of all phonon modes. As an example, Fig. 3 shows the residual of the PGD iteration process of an ordinary phonon wave vector ($0.03\ Å^{-1}$, $0.07\ Å^{-1}$, and $0.1\ Å^{-1}$) in the amorphous interface. The iteration achieves convergence within 100 iterations. Using ten distinct random initial estimates, we find that they all converge to the same global minimum and exhibit similar convergence speeds. This result validates the stability and efficiency of the PGD iteration.

We then examine the localized effects in the LD method. In the derivation, we have assumed that the device is sufficiently thick so that all localized effects remain within it. Here, we examine the

TABLE I. The TBC of three types of Si/Ge interfaces at 300 K using the original and robust lattice dynamics method, compared with results from the literature.

Method	Atomically smooth interface ($MW/m^2 K$)	Interdiffusion interface	Amorphous interface
Robust LD	324	288 $MW/m^2 K$	136 $MW/m^2 K$
Original LD	323	Failed	Failed
Original LD[38]	320	None	None
AGF[49]	280	None	None
NEMD[11]	310	None	None

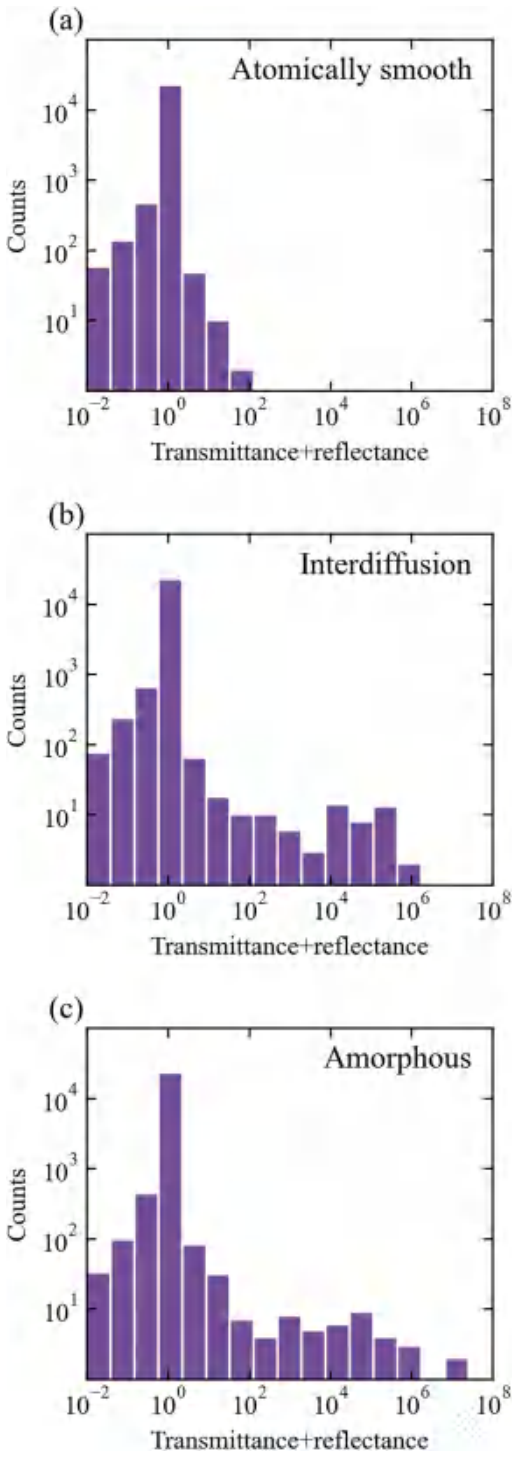

FIG. 2. Histograms of the sum of transmittance and reflectance for each phonon mode used in the calculation of TBC using the original LD method. (a) The atomically smooth interface. (b) The interdiffusion interface. (c) The amorphous interface.

localized component to verify the assumption. The localized component is determined by subtracting the bulk phonon components from the eigenvectors of atoms in the device, depending on their relative position to the interface, that is,

$$u_{local} = \begin{cases} u_i - \left(s_I e^{iq_i \cdot r_i} + \sum_{R_j} A_{R_j} s_{R_j} e^{iq_{R_j} \cdot r_i} \right), & i \in \text{Si}, \\ u_i - \sum_{T_k} A_{T_k} s_{T_k} e^{iq_{T_k} \cdot r_i}, & i \in \text{Ge}: \end{cases} \tag{20}$$

As an example, Fig. 4(a) shows the localized component of a traverse acoustic phonon with a frequency of 5 THz and a wave vector of (0, 0, 1 nm^{-1}) at the atomically smooth interface. The transmittance of this phonon mode is zero, which means that it is experiencing total reflection. The localized evanescent mode situated on the Ge side is exposed, which exponentially decays to zero within a distance of 4 nm. In contrast, the localized components of most other phonon modes with nonzero transmittance are limited to much shorter distances. Therefore, the device region with a thickness of 10 nm is deemed sufficient. Furthermore, we have tested the convergence of the TBC by extending the thickness of the device, as depicted in Fig. 4(b), which confirms the same conclusion.

From an alternative perspective, the local density of states (LDOS) captures the localized effects near the interface. To calculate the LDOS from the LD method, we perform a uniform sampling on Si and Ge phonon modes in their first Brillouin zones and regard them as incident phonons. Then, we compute the resulting eigenvectors of atoms in the device and sum up the squares of magnitudes of these eigenvectors over all sampling points, multiplied by a factor of

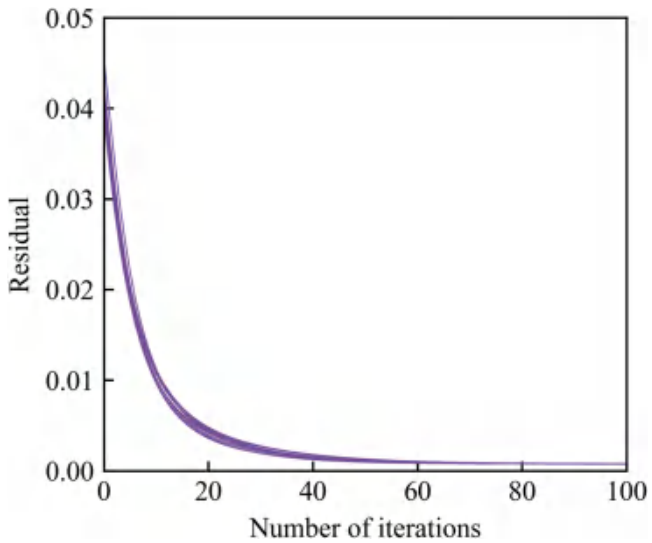

FIG. 3. The iterative convergence of the PGD method with ten random initial guesses carried out at an ordinary phonon wave vector (0.03 $Å^{-1}$, 0.07 $Å^{-1}$, and 0.1 $Å^{-1}$) in a rough Si/Ge interface with an amorphous layer of 1 nm.

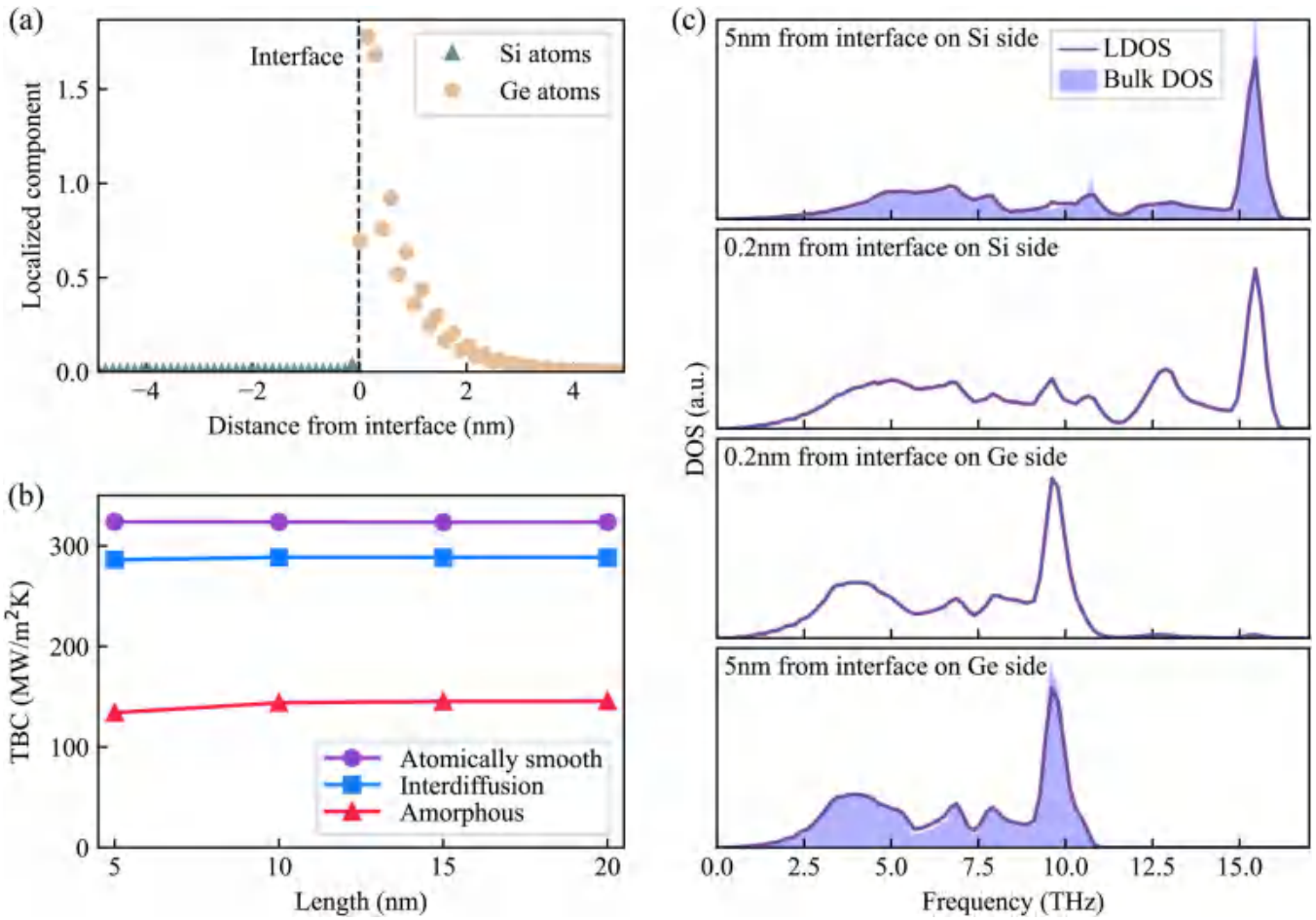

FIG. 4. (a) The localized component of a traverse acoustic phonon with a frequency of 5 THz and a wave vector of (0, 0, 1 nm^{-1}) which incident on the atomically smooth Si/Ge surface. (b) The calculated TBC at various lengths of the device. (c) The solid lines represent the LDOS of four distinct atoms located in the device with varying distances from the interface. The shaded regions in the top and bottom panels represent the DOS of bulk Si and Ge, respectively.

the delta function. The LDOS of atom i in the device is

$$\mathrm{LDOS}_i(\omega) = \sum_{q \text{ in Si BZ}} |u_i|^2 \delta(\omega - \omega_q) + \sum_{q \text{ in Ge BZ}} |u_i|^2 \delta(\omega - \omega_q): \tag{21}$$

The LDOS of four distinct atoms located in the device with varying distances from the interface is shown in Fig. 4(c). It can be seen that the LDOS of atoms in the vicinity of the interface differs from that of the bulk DOS. On the Si side, a peak in the LDOS emerges around 10 THz, which is absent in the bulk DOS. This can be attributed to the influence of the DOS peak of optical phonons in Ge at the same frequency. While on the Ge side, peaks appear in the LDOS above the cutoff frequency within the range of 12–15 THz. These peaks are the results of the influence of phonons in Si. On the other hand, the LDOS of atoms located far away from the interface approximates the bulk DOS. Therefore, the localized effects are confined to a narrow region near the interface. Our results are consistent with the LDOS from molecular dynamics.[22] From the evanescent modes and LDOS, it can be observed that our approach accurately captures the interface effects while employing a sufficiently large device thickness. It is worth emphasizing that, compared to LDOS calculations using molecular dynamics, our method provides more comprehensive insights into the interface effects, as it reveals the interface effects of each phonon mode individually.

The most notable advantage of the LD method over MD and AGF methods lies in its ability to compute the mode-resolved phonon transmittance. The AGF method is limited to calculating the transmittance of phonons with discrete wave vectors,[22] while the wave packet method based on MD can only compute the transmittance of phonons with vertically incident angles.[52] Here, we present the results of the LD approach taking the atomically smooth interface as an example, Figs. 5(a) and 5(b) show the transmittance of Si and Ge phonons along high-symmetry paths, respectively. Figure 5(c)

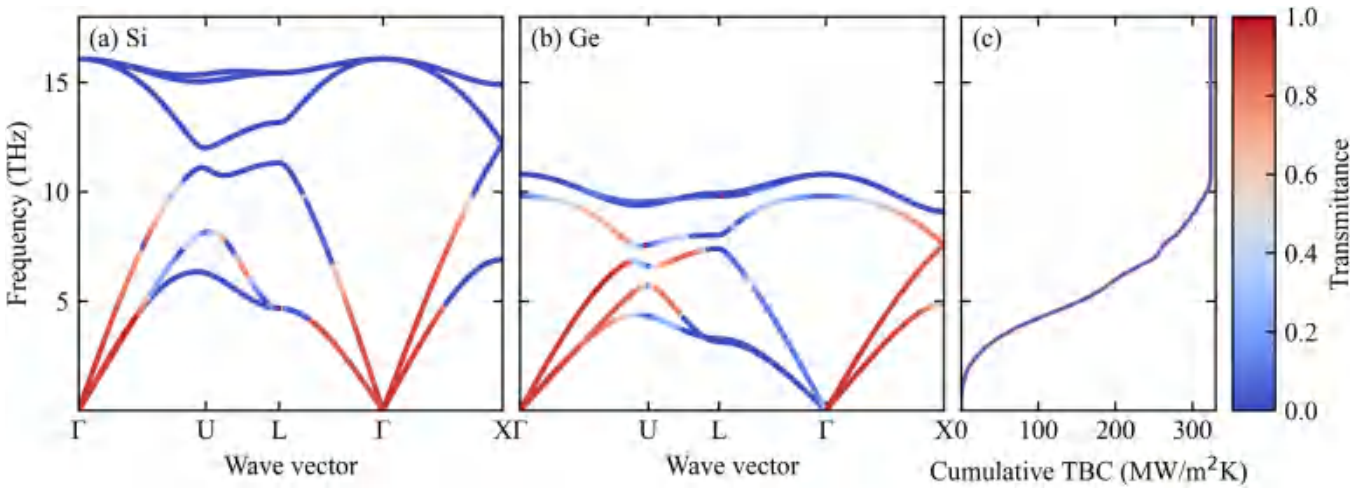

FIG. 5. (a) The transmittance of Si phonons along high-symmetry paths. (b) The transmittance of Ge phonons along high-symmetry paths. Although Ge is strained, we still adopt the high-symmetry paths of the unstrained structure in order to compare with Si. (c) The cumulative frequency-dependent TBC.

shows the cumulative frequency-dependent TBC, which aligns with the results from AGF[53] and NEMD.[54] The transmittance of Si and Ge phonons exhibit striking dissimilarities. On one hand, the Si phonons exhibit nearly isotropic transmittance. All optical phonon modes of Si have zero transmittance because their frequencies exceed the cutoff frequency of Ge. The majority of TBC is contributed by the acoustic phonons, as seen in Fig. 5(c). On the other hand, the Ge phonons exhibit anisotropic transmittance. The transmittance along Γ–L is significantly lower than that along Γ–U and Γ–X. The reason is that phonons along Γ–L have a larger incident angle. Since the speed of sound is lower in Ge than Si, phonons with larger incident angles are experiencing total reflection. The phonon transmittance along high-symmetry paths provides an overall characterization of the phonon transmission. The computed results align with theoretical predictions, particularly by accurately capturing the phenomenon of total internal reflection at large incident angles.

Next, we compute the statistical characteristics of the phonon transmittance on a uniformly sampled grid in the Brillouin zone, thereby gaining a deeper understanding of the characteristics of phonon transmittance. We define the average phonon transmittance as a function of the frequency ω, the incident polar angle θ, and the incident azimuth angle f. The angles of the incident phonons are defined by their group velocities rather than their wave vectors. The average transmittance of phonons is calculated through a weighted average using the Landauer formula. For example,

$$\bar{\mathrm{T}}(\omega) = \frac{\sum_{\mathrm{q},\nu} \hbar\omega_{\mathrm{q}\nu} v_{\mathrm{q}\nu,z} \mathrm{T}_{\mathrm{q}\nu} \frac{\partial \mathrm{f}}{\partial \mathrm{T}} \delta\left(\omega_{\mathrm{q}\nu} - \omega\right)}{\sum_{\mathrm{q},\nu} \hbar\omega_{\mathrm{q}\nu} v_{\mathrm{q}\nu,z} \frac{\partial \mathrm{f}}{\partial \mathrm{T}} \delta\left(\omega_{\mathrm{q}\nu} - \omega\right)},$$
$$\bar{\mathrm{T}}(\omega, \theta) = \frac{\sum_{\mathrm{q},\nu} \hbar\omega_{\mathrm{q}\nu} v_{\mathrm{q}\nu,z} \mathrm{T}_{\mathrm{q}\nu} \frac{\partial \mathrm{f}}{\partial \mathrm{T}} \delta\left(\omega_{\mathrm{q}\nu} - \omega, \theta_{\mathrm{q}\nu} - \theta\right)}{\sum_{\mathrm{q},\nu} \hbar\omega_{\mathrm{q}\nu} v_{\mathrm{q}\nu,z} \frac{\partial \mathrm{f}}{\partial \mathrm{T}} \delta\left(\omega_{\mathrm{q}\nu} - \omega, \theta_{\mathrm{q}\nu} - \theta\right)}, \quad (22)$$

and $\bar{\mathrm{T}}(\theta)$, $\bar{\mathrm{T}}(f)$, $\bar{\mathrm{T}}(\omega, f)$, and $\bar{\mathrm{T}}(\theta, f)$ are defined similarly. For the convenience of visualization, we consider the simplest form of one and two variables. According to the definition, the average phonon transmittance can precisely reproduce the total TBC,

$$\mathrm{G} = \frac{1}{\mathrm{V}} \sum_{\mathrm{q},\nu} \hbar\omega_{\mathrm{q}\nu} v_{\mathrm{q}\nu,z} \mathrm{T}_{\mathrm{q}\nu} \frac{\partial \mathrm{f}}{\partial \mathrm{T}} = \frac{1}{\mathrm{V}} \sum_{\mathrm{q},\nu} \hbar\omega_{\mathrm{q}\nu} v_{\mathrm{q}\nu,z} \bar{\mathrm{T}} \frac{\partial \mathrm{f}}{\partial \mathrm{T}}. \quad (23)$$

It is worth noting that other models for phonon transmittance, such as the AMM[12] and DMM,[55] rely on assumptions, whereas our model does not. Our approach follows a bottom-up method, summarizing statistical regularities from mode-resolved phonon transmittance in a more detailed manner to accurately calculate the TBC from the outset. By analyzing the statistical characteristics of phonon transmittance, a more in-depth understanding of the physical mechanisms governing phonon behavior at interfaces can be attained.

All six dependency relations of $\bar{\mathrm{T}}$ are shown in Fig. 6. By comparing the dependencies of the average phonon transmittance on three individual variables, as shown in Figs. 6(a)–6(c), it can be observed that the frequency has the most significant impact on the transmittance, followed by the incident angle, and finally the azimuthal angle. As presented in Fig. 6(a), the average phonon transmittance is relatively high and consistent in the low-frequency region, and it sharply decreases with increasing frequency. Figure 6(b) demonstrates that the transmittance decreases with the increase of the polar angle. Figure 6(c) highlights the anisotropic behavior of transmittance with respect to the azimuth angle, demonstrating approximately mirrored symmetry in two perpendicular directions, which arises from the symmetry in the [001] direction of the diamond structure of Si and Ge. Despite such anisotropy, we can ignore the slight influence of azimuth angles by averaging when considering only the values of TBC. The dependence of phonon transmittance on phonon frequency has already reached a

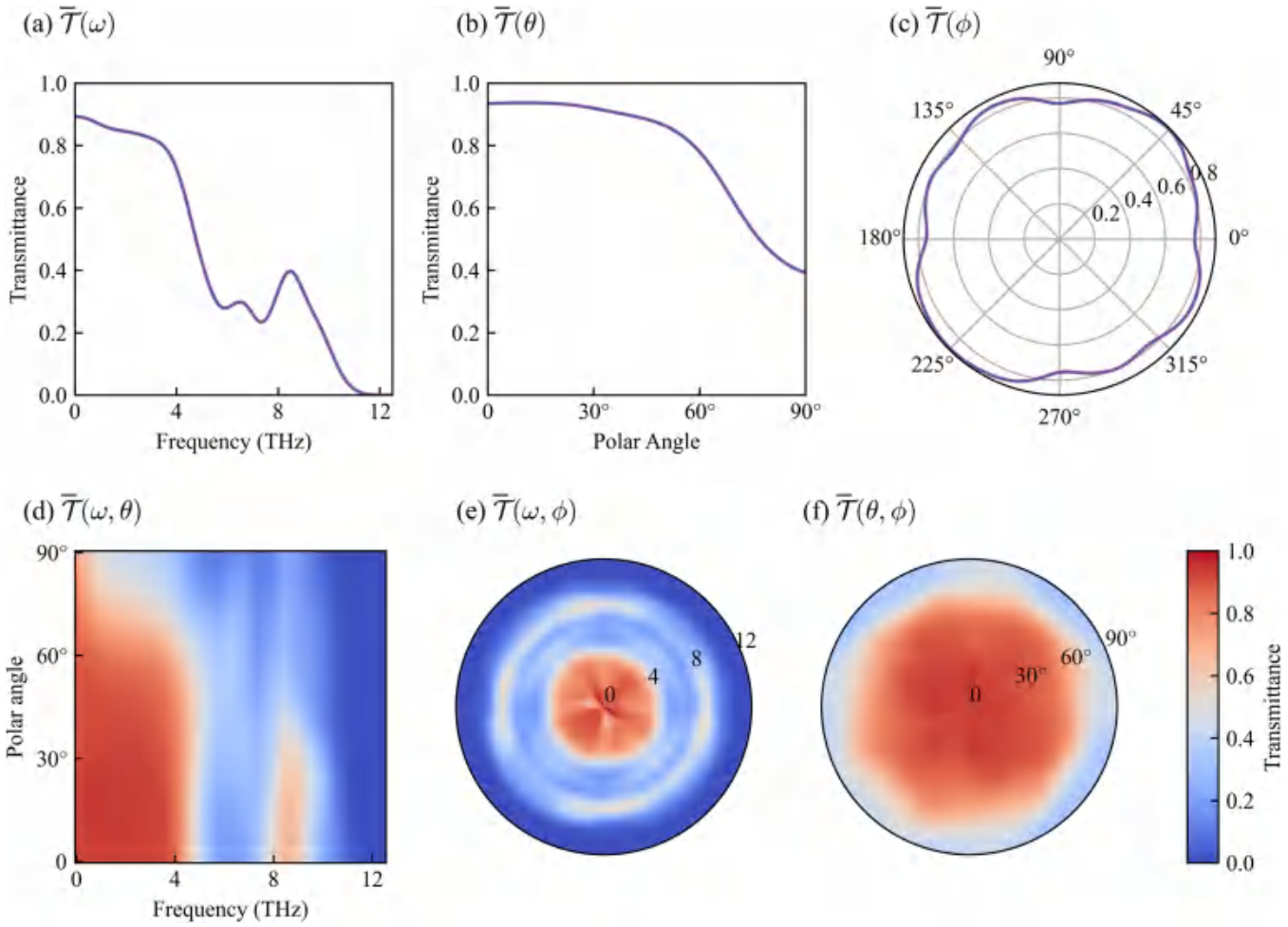

FIG. 6. The average transmittance defined on one or two variables. (a) $\bar{T}(\omega)$, (b) $\bar{T}(\theta)$, (c) $\bar{T}(f)$, (d) $\bar{T}(\omega, \theta)$, (e) $\bar{T}(\omega, f)$, and (f) $\bar{T}(\theta, f)$. Among them, $\bar{T}(\theta)$, $\bar{T}(f)$, and $\bar{T}(\theta, f)$ are averaged on phonons with frequencies lower than 4 THz.

consensus.[46,55] However, our work further demonstrates that in highly isotropic materials such as Si and Ge, the transmittance of incident phonons is generally independent of the azimuthal angle but exhibits a significant dependence on the polar angle.

Figures 6(d)–6(f) present the dependency of $\bar{T}$ on two variables, which strengthens our previous conclusion. Figure 6(d) reveals the influence of frequency and incident angle as coupled factors on the average phonon transmittance. Figures 6(e) and 6(f) provide further evidence of the negligible anisotropy in the azimuthal angle by showcasing the joint distribution of the phonon transmittance with respect to frequency, incident angle, and azimuthal angle. Therefore, we can make the approximation that the average transmittance relies only on ω and θ, that is,

$$\bar{T}(\omega, \theta, f) \approx \bar{T}(\omega, \theta): \tag{24}$$

Further observation of Fig. 6(d) reveals that the transmittance decreases as the polar angle increases, with a similar rate of decrease across different frequencies. Therefore, it can be assumed that the effects of frequency and polar angle on the transmittance are decoupled, i.e.,

$$\bar{T}(\omega, \theta) \approx \bar{T}_0(\omega) g(\theta), \tag{25}$$

in which $\bar{T}_0(\omega) ; \bar{T}(\omega, 0)$ is the transmittance of phonons with the zero incident angle. The factor of polar angle is defined as

$$g(\theta) = \frac{\bar{T}(\theta)}{\bar{T}(\theta)|_{\theta=0}}: \tag{26}$$

Figure 7 compares the coupled expression $\bar{T}(\omega, \theta)$ with the decoupled expression $\bar{T}_0(\omega) g(\theta)$ in the atomically smooth interface, interdiffusion interface, and amorphous interface. The TBC obtained from each expression is indicated in each subfigure. The TBC values in Figs. 7(a)–7(c) align with those in Table I, indicating

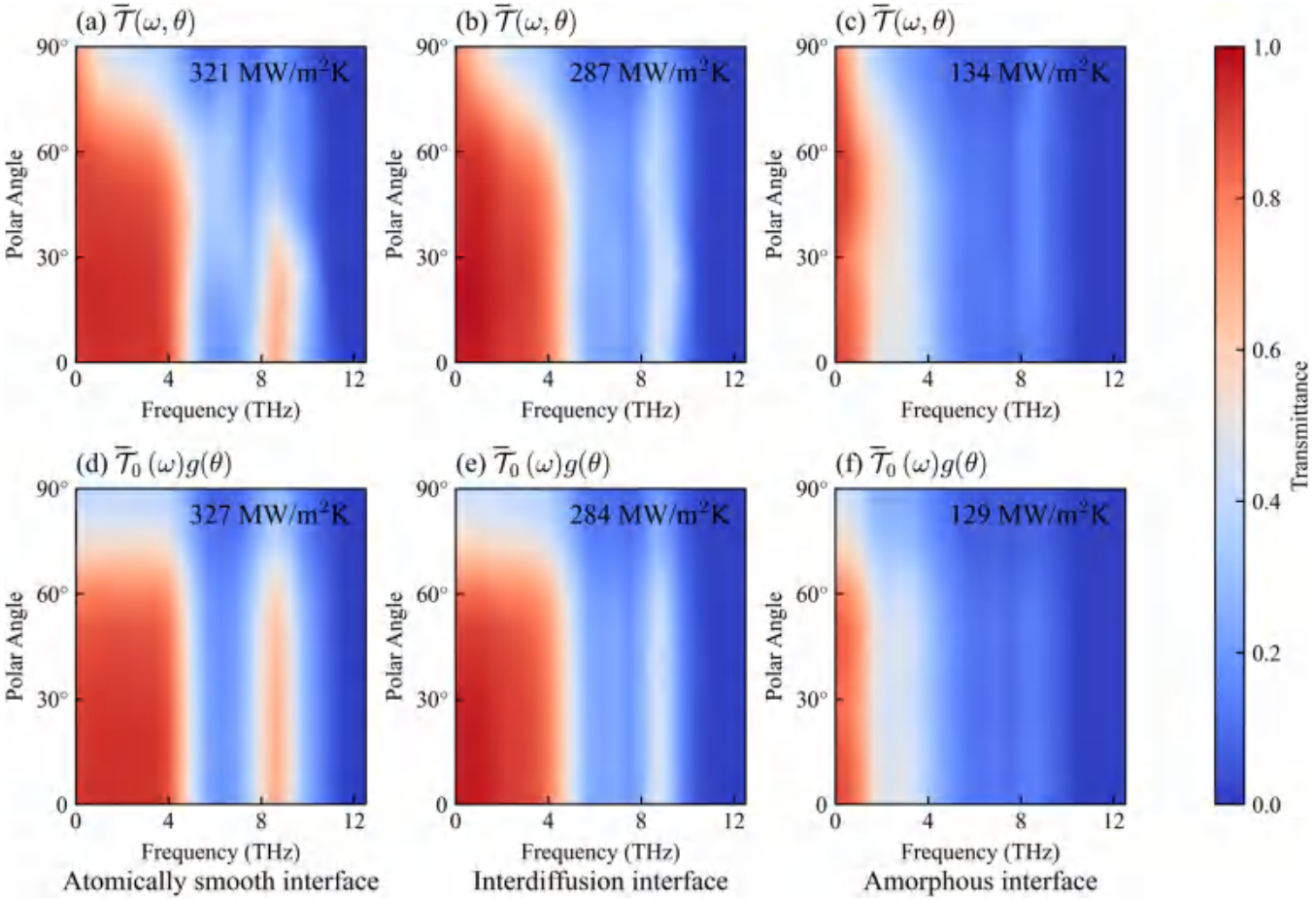

FIG. 7. The coupled average transmittance [(a)–(c)] and the decoupled average transmittance [(d)–(f)] in the atomically smooth interface, the interdiffusion interface, and the amorphous interface. The TBC for each configuration is presented in each subfigure.

that the average phonon transmittance reproduces the precise TBC. This validates the conclusion of Eq. (23). By comparing Figs. 7(a) and 7(d), it can be observed that the phonon transmittance distribution of the decoupled expression bears resemblance to that of the coupled one, and similar TBC values are computed as well. By further comparing Fig. 7(b) with Fig. 7(e) and Fig. 7(c) with Fig. 7(f), the same conclusion can be drawn. Both the coupled expression and the decouple one reproduce the TBC precisely, while the decouple one has a much simpler form. Hence, the decoupled expression is applicable to atomically smooth Si/Ge interfaces, interdiffusion interfaces, and amorphous interfaces.

In summary, our model of phonon transmittance will advance the understanding of the underlying mechanisms of TBC. On one hand, while previous models primarily focused on the influence of phonon frequencies on transmittance, our model takes into account the impact of phonon incident angles, benefiting from the calculation of mode-resolved phonon transmittance. On the other hand, our model relies solely on the atomic structure of the interface, without any assumptions or predefined parameters, enabling a bottom-up computation approach. It is important to emphasize that the specific expression of the phonon transmittance depends on the types of materials on both sides of the interface and the atomic structure of the interface itself. Therefore, it is impossible to summarize all situations with a universal formula. However, the characteristics of the phonon transmittance, such as weak anisotropy in azimuth angle and decoupling with respect to frequency and polar angle, will generally apply to interfaces composed of simple materials.

IV. CONCLUSIONS

This paper presents a robust LD approach for computing mode-resolved phonon transmittance at interfaces, addressing the issue of the absence of energy conservation constraint in the original LD approach. The constraint of energy conservation is achieved using linear algebra transformations and projection gradient

descent iterations. Our method shows agreement with the original LD approach when applied to the atomically smooth Si/Ge interface, while also displaying robustness when dealing with rough Si/Ge interfaces. Our approach captures the localized effect at the interfaces. The evanescent mode is exposed by examining the localized component of atom motion. Using a bottom-up approach, the statistical characteristics of transmittance based on mode-resolved values are analyzed, taking frequency, polar angle, and azimuth angle into consideration as influencing factors. Results show that the anisotropy in the azimuth angle can be ignored, and the dependency on the frequency and polar angle can be decoupled. The decoupled expression accurately reproduces the TBC calculated with mode-resolved transmittance. The method presented in this paper facilitates the exploration of TBC mechanisms in rough interfaces and offers opportunities to investigate the relationship between TBC and atomic structures.

ACKNOWLEDGMENTS

This work was supported by the National Natural Science Foundation of China (Grant Nos. 51825601, U20A20301, and 52250273).

AUTHOR DECLARATIONS

Conflict of Interest

The authors have no conflicts to disclose.

Author Contributions

Hong-Ao Yang: Conceptualization (equal); Data curation (equal); Formal analysis (equal); Investigation (equal); Methodology (equal); Software (equal); Validation (equal); Visualization (equal); Writing – original draft (equal); Writing – review & editing (equal). Bing-Yang Cao: Funding acquisition (equal); Project administration (equal); Supervision (equal); Writing – review & editing (equal).

DATA AVAILABILITY

The data that support the findings of this study are available from the corresponding author upon reasonable request.

REFERENCES

[1]A. Sarua, H. Ji, K. P. Hilton, D. J. Wallis, M. J. Uren, T. Martin, and M. Kuball, "Thermal boundary resistance between GaN and substrate in AlGaN/GaN electronic devices," IEEE Trans. Electron Devices 54(12), 3152–3158 (2007).
[2]E. A. Scott, J. T. Gaskins, S. W. King, and P. E. Hopkins, "Thermal conductivity and thermal boundary resistance of atomic layer deposited high-k dielectric aluminum oxide, hafnium oxide, and titanium oxide thin films on silicon," APL Mater. 6(5), 058302 (2018).
[3]X.-D. Zhang, G. Yang, and B.-Y. Cao, "Bonding-enhanced interfacial thermal transport: Mechanisms, materials, and applications," Adv. Mater. Interfaces 9(27), 2200078 (2022).
[4]X. Qian, J. Zhou, and G. Chen, "Phonon-engineered extreme thermal conductivity materials," Nat. Mater. 20(9), 1188–1202 (2021).
[5]D. Guo, Q. Guo, Z. Chen, Z. Wu, P. Li, and W. Tang, "Review of Ga_2O_3-based optoelectronic devices," Mater. Today Phys. 11, 100157 (2019).
[6]P. E. Hopkins, "Thermal transport across solid interfaces with nanoscale imperfections: Effects of roughness, disorder, dislocations, and bonding on thermal boundary conductance," Int. Sch. Res. Not. 2013, e682586 (2013).
[7]M. Blank and L. Weber, "Influence of interfacial structural disorder and/or chemical interdiffusion on thermal boundary conductance for Ti/Si and Au/Si couples," J. Appl. Phys. 126(15), 155302 (2019).
[8]R. Xie, J. Tiwari, and T. Feng, "Impacts of various interfacial nanostructures on spectral phonon thermal boundary conductance," J. Appl. Phys. 132(11), 115108 (2022).
[9]M. D. Losego, M. E. Grady, N. R. Sottos, D. G. Cahill, and P. V. Braun, "Effects of chemical bonding on heat transport across interfaces," Nat. Mater. 11(6), 502–506 (2012).
[10]A. Giri, S. W. King, W. A. Lanford, A. B. Mei, D. Merrill, L. Li, R. Oviedo, J. Richards, D. H. Olson, J. L. Braun, J. T. Gaskins, F. Deangelis, A. Henry, and P. E. Hopkins, "Interfacial defect vibrations enhance thermal transport in amorphous multilayers with ultrahigh thermal boundary conductance," Adv. Mater. 30(44), 1804097 (2018).
[11]E. S. Landry and A. J. H. McGaughey, "Thermal boundary resistance predictions from molecular dynamics simulations and theoretical calculations," Phys. Rev. B 80(16), 165304 (2009).
[12]W. A. Little, "The transport of heat between dissimilar solids at low temperatures," Can. J. Phys. 37(3), 334–349 (1959).
[13]E. T. Swartz and R. O. Pohl, "Thermal resistance at interfaces," Appl. Phys. Lett. 51(26), 2200–2202 (1987).
[14]P. Reddy, K. Castelino, and A. Majumdar, "Diffuse mismatch model of thermal boundary conductance using exact phonon dispersion," Appl. Phys. Lett. 87(21), 211908 (2005).
[15]J. C. Duda, T. E. Beechem, J. L. Smoyer, P. M. Norris, and P. E. Hopkins, "Role of dispersion on phononic thermal boundary conductance," J. Appl. Phys. 108(7), 073515 (2010).
[16]T. Beechem and P. E. Hopkins, "Predictions of thermal boundary conductance for systems of disordered solids and interfaces," J. Appl. Phys. 106(12), 124301 (2009).
[17]P. E. Hopkins, "Multiple phonon processes contributing to inelastic scattering during thermal boundary conductance at solid interfaces," J. Appl. Phys. 106(1), 013528 (2009).
[18]R. Cheaito, J. T. Gaskins, M. E. Caplan, B. F. Donovan, B. M. Foley, A. Giri, J. C. Duda, C. J. Szwejkowski, C. Constantin, H. J. Brown-Shaklee, J. F. Ihlefeld, and P. E. Hopkins, "Thermal boundary conductance accumulation and interfacial phonon transmission: Measurements and theory," Phys. Rev. B 91(3), 035432 (2015).
[19]C. Hua, X. Chen, N. K. Ravichandran, and A. J. Minnich, "Experimental metrology to obtain thermal phonon transmission coefficients at solid interfaces," Phys. Rev. B 95(20), 205423 (2017).
[20]J.-S. Wang, J. Wang, and N. Zeng, "Nonequilibrium Green's function approach to mesoscopic thermal transport," Phys. Rev. B 74(3), 033408 (2006).
[21]W. Zhang, T. S. Fisher, and N. Mingo, "The atomistic Green's function method: An efficient simulation approach for nanoscale phonon transport," Numer. Heat Transf. Part B Fundam. 51(4), 333–349 (2007).
[22]A. Giri and P. E. Hopkins, "A review of experimental and computational advances in thermal boundary conductance and nanoscale thermal transport across solid interfaces," Adv. Funct. Mater. 30(8), 1903857 (2020).
[23]Y. Guo, Z. Zhang, M. Bescond, S. Xiong, M. Nomura, and S. Volz, "Anharmonic phonon-phonon scattering at the interface between two solids by nonequilibrium Green's function formalism," Phys. Rev. B 103(17), 174306 (2021).
[24]Y. Chalopin, N. Mingo, J. Diao, D. Srivastava, and S. Volz, "Large effects of pressure induced inelastic channels on interface thermal conductance," Appl. Phys. Lett. 101(22), 221903 (2012).
[25]Y. Chalopin and S. Volz, "A microscopic formulation of the phonon transmission at the nanoscale," Appl. Phys. Lett. 103(5), 051602 (2013).
[26]K. Sääskilahti, J. Oksanen, J. Tulkki, and S. Volz, "Role of anharmonic phonon scattering in the spectrally decomposed thermal conductance at planar interfaces," Phys. Rev. B 90(13), 134312 (2014).

[27]Y. Zhou and M. Hu, "Quantitatively analyzing phonon spectral contribution of thermal conductivity based on nonequilibrium molecular dynamics simulations. II. From time Fourier transform," Phys. Rev. B 92(19), 195205 (2015).
[28]J.-L. Barrat and F. Chiaruttini, "Kapitza resistance at the liquid–solid interface," Mol. Phys. 101(11), 1605–1610 (2003).
[29]K. Gordiz and A. Henry, "A formalism for calculating the modal contributions to thermal interface conductance," New J. Phys. 17, 103002 (2015).
[30]Z. Liang and P. Keblinski, "Finite-size effects on molecular dynamics interfacial thermal-resistance predictions," Phys. Rev. B 90(7), 075411 (2014).
[31]Z.-Y. Ong and G. Zhang, "Efficient approach for modeling phonon transmission probability in nanoscale interfacial thermal transport," Phys. Rev. B 91(17), 174302 (2015).
[32]B. Latour, N. Shulumba, and A. J. Minnich, "Ab initio study of mode-resolved phonon transmission at Si/Ge interfaces using atomistic Green's functions," Phys. Rev. B 96(10), 104310 (2017).
[33]Q. Song, and G. Chen, "Evaluation of the diffuse mismatch model for phonon scattering at disordered interfaces," Phys. Rev. B 104(8), 085310 (2021).
[34]L. Yang, B. Latour, and A. J. Minnich, "Phonon transmission at crystalline-amorphous interfaces studied using mode-resolved atomistic Green's functions," Phys. Rev. B 97(20), 205306 (2018).
[35]Z.-Y. Ong, "Tutorial: Concepts and numerical techniques for modeling individual phonon transmission at interfaces," J. Appl. Phys. 124(15), 151101 (2018).
[36]M. E. Lumpkin, W. M. Saslow, and W. M. Visscher, "One-dimensional Kapitza conductance: Comparison of the phonon mismatch theory with computer experiments," Phys. Rev. B 17(11), 4295–4302 (1978).
[37]D. A. Young and H. J. Maris, "Lattice-dynamical calculation of the Kapitza resistance between fcc lattices," Phys. Rev. B 40(6), 3685–3693 (1989).
[38]H. Zhao and J. B. Freund, "Lattice-dynamical calculation of phonon scattering at ideal Si–Ge interfaces," J. Appl. Phys. 97(2), 024903 (2005).
[39]J. Wang and J.-S. Wang, "Mode-dependent energy transmission across nanotube junctions calculated with a lattice dynamics approach," Phys. Rev. B 74(5), 054303 (2006).
[40]L. Zhang, P. Keblinski, J.-S. Wang, and B. Li, "Interfacial thermal transport in atomic junctions," Phys. Rev. B 83(6), 064303 (2011).
[41]S. Lu and A. J. H. McGaughey, "Thermal conductance of superlattice junctions," AIP Adv. 5(5), 053205 (2015).
[42]A. Alkurdi, S. Pailhès, and S. Merabia, "Critical angle for interfacial phonon scattering: Results from ab initio lattice dynamics calculations," Appl. Phys. Lett. 111(9), 093101 (2017).
[43]J.-S. Wang, J. Wang, and J. T. Lü, "Quantum thermal transport in nanostructures," Eur. Phys. J. B 62(4), 381–404 (2008).
[44]S. P. Boyd and L. Vandenberghe, Convex Optimization (Cambridge University Press, 2004).
[45]T. Vu and R. Raich, "On asymptotic linear convergence of projected gradient descent for constrained least squares," IEEE Trans. Signal Process 70, 4061–4076 (2022).
[46]J. Chen, X. Xu, J. Zhou, and B. Li, "Interfacial thermal resistance: Past, present, and future," Rev. Mod. Phys. 94(2), 025002 (2022).
[47]V. Popescu and A. Zunger, "Effective band structure of random alloys," Phys. Rev. Lett. 104(23), 236403 (2010).
[48]K. R. Hahn, M. Puligheddu, and L. Colombo, "Thermal boundary resistance at Si/Ge interfaces determined by approach-to-equilibrium molecular dynamics simulations," Phys. Rev. B 91(19), 195313 (2015).
[49]Z. Tian, K. Esfarjani, and G. Chen, "Enhancing phonon transmission across a Si/Ge interface by atomic roughness: First-principles study with the Green's function method," Phys. Rev. B 86(23), 235304 (2012).
[50]J. Tersoff, "Modeling solid-state chemistry: Interatomic potentials for multicomponent systems," Phys. Rev. B 39(8), 5566–5568 (1989).
[51]A. Togo and I. Tanaka, "First principles phonon calculations in materials science," Scr. Mater. 108, 1–5 (2015).
[52]P. K. Schelling, S. R. Phillpot, and P. Keblinski, "Phonon wave-packet dynamics at semiconductor interfaces by molecular-dynamics simulation," Appl. Phys. Lett. 80(14), 2484–2486 (2002).
[53]K. Gordiz and A. Henry, "Phonon transport at interfaces between different phases of silicon and germanium," J. Appl. Phys. 121(2), 025102 (2017).
[54]Y. Zhou and M. Hu, "Full quantification of frequency-dependent interfacial thermal conductance contributed by two- and three-phonon scattering processes from nonequilibrium molecular dynamics simulations," Phys. Rev. B 95(11), 115313 (2017).
[55]E. T. Swartz and R. O. Pohl, "Thermal boundary resistance," Rev. Mod. Phys. 61(3), 605–668 (1989).